The anisotropic interaction potential of D2Ne from statetostate differential cross sections for rotational excitation

J. Andres, U. Buck, F. Huisken, J. Schleusener, and F. Torello

Citation: The Journal of Chemical Physics **73**, 5620 (1980); doi: 10.1063/1.440084
View online: http://dx.doi.org/10.1063/1.440084
View Table of Contents: http://scitation.aip.org/content/aip/journal/jcp/73/11?ver=pdfcov
Published by the AIP Publishing

The anisotropic interaction potential of D_2Ne from state-to-state differential cross sections for rotational excitation

J. Andres, U. Buck, F. Huisken, J. Schleusener, and F. Torello[a)]

Max-Planck-Institut für Strömungsforschung, D3400 Göttingen, Federal Republic of Germany
(Received 15 June 1980; accepted 13 August 1980)

Differential cross sections for the rotational excitation from $j = 0$ to $j = 2$ of D_2 scattered by Ne have been measured at an energy of $E = 84.9$ meV. The experiments have been performed in a crossed nozzle beam apparatus with time-of-flight analysis of the scattered particles using the pseudorandom chopper method. A detailed analysis of the experimental data which are peaked in the backward direction showed that they are mainly sensitive to the repulsive part of the pure anisotropic potential. From a combined analysis of the state-to-state differential cross sections of the $j = 0$ to $j = 0$ and the $j = 0$ to $j = 2$ transition of $D_2 + Ne$ and the $j = 0$ to $j = 1$ transition of $HD + Ne$ previously measured, the complete potential energy surface for the hydrogen–neon system is obtained using the coupled states method. The anisotropic contribution varies from 37% of the isotropic part in the repulsive region (2.4 Å) to 12% in the attractive region (3.5 Å). The results differ from the other potential models derived for this system from calculations, spectroscopic studies, and bulk properties. However, it is in agreement with the results of a recently developed inversion method based on the exponential distorted wave approximation using the same experimental data.

I. INTRODUCTION

Rotational energy transfer is one of the most important processes in molecular dynamics. Thus considerable effort has been devoted to the use of molecular beam techniques to investigate these collision processes measuring cross sections for resolved state-to-state transitions. Until very recently, such measurements were limited to a few energy loss studies for ion–molecule systems, or polar molecules involving electric quadrupole state selection and detection.[1] A review of measurements of the total scattering cross section with state-selected beams without energy transfer is given in Ref. 2. The advent of new laser techniques allowed extension of the method to the measurement of state-to-state integral cross sections for LiH scattered from a number gases[3] and state-to-state differential cross sections for $Na_2 + Ne$.[4] Recently interesting structure in the differential cross section for unresolved rotational transitions has been reported.[5,6] Energy loss studies with single resolved rotational transitions for pure neutral systems have been obtained for HD + Ne (Ref. 7), HD + He (Ref. 8), HD + HD (Ref. 9), and HD + D_2 (Ref. 10).

All these systems which contain a hydrogen molecule scattering partner can be considered as prototype examples for studying the fundamental interaction of this simple molecule with other atoms and molecules. The widely spaced rotational energy levels favor the resolution of single rotational transitions. From a theoretical point of view, the number of states required in a basis set for an exact quantum calculation is relatively small, so that it is easy to use theoretical procedures and to test approximations for the calculation of rotationally inelastic cross sections. Thus it is possible to derive the underlying anisotropic interaction responsible for rotational transitions and to compare the results to potential energy surfaces obtained from *ab initio* calculations that are feasible for these small systems. Unfortunately, in most cases the $0 \rightarrow 1$ transition of the HD molecule was measured because of its comparatively large transition probability. Although this transition has its own merits as a prototype for a mass asymmetric system, a detailed study of the sensitivity of the inelastic cross section to the interaction potential indicates that the anisotropic potential of the HD systems responsible for the $0 \rightarrow 1$ transition is mainly due to a shift of the center of mass from the center of symmetry and much less due to the anisotropy of the interaction that is present for the symmetric molecules.[11] Thus the measurement of the $\Delta j = 2$ transition is necessary as a direct probe for the anisotropy of the mass-symmetric hydrogen molecule systems. Recently, time-of-flight distributions for such transitions were presented for $D_2 + He$ (Ref. 12), $D_2 + Ne$ (Ref. 13), and $HD + D_2$ (Refs. 12 and 13).

In this paper, we report differential cross section results for $j = 0$ to $j = 0$ and $j = 0$ to $j = 2$ of D_2 molecules scattered by Ne atoms at an energy of $E = 84.9$ meV between 37° and 108° in the center of mass system. The experiments have been performed for *ortho*(o)-D_2 which contains only the even j values and normal(n)-D_2 which consists of $\frac{2}{3}$ o-D_2 and $\frac{1}{3}$ p-D_2 where only the odd j values are present.

The present experimental results for the $0 \rightarrow 2$ transition of $D_2 + Ne$ are used together with the differential cross section for the $0 \rightarrow 1$ transition for HD + Ne (Ref. 11), the total differential cross section for $D_2 + Ne$ (Ref. 14), and the velocity dependence of integral cross sections for $H_2 + Ne$ with oriented H_2 molecules[15] to give the first determination of the complete potential surface—isotropic and anisotropic. The result of this fitting procedure based on coupled states calculations is then compared with other potentials for this system obtained from model calculations,[16] the spectroscopy of van der Waals complexes,[17,18] bulk relaxation data[19] and a direct inversion procedure based on the exponential distorted wave approximation but using the same experimental data.[20]

In Sec. II we give a short description of the experimental arrangement. Our experimental results for the

[a)]Permanent address: Istituto di Scienze Fisiche, Viale Benedetto XV, 5, Genova, Italy.

 0021-9606/80/235620-11$01.00

TABLE I. Beam parameters.

	o-D_2	n-D_2	Ne
Nozzle diameter (mm)	0.01	0.01	0.05
Source pressure (bar)	195	195	18
Source temperature (K)	300	300	300
Peak velocity (m/s)	2063	2050	800
Velocity distribution $\Delta v/v$ (%)	4.5	4.5	3.9
Rotational temperature (K)	70	62	...
Fraction in $j=0$	0.89	0.62	...
$j=1$	...	0.33	...
$j=2$	0.11	0.05	...

$0 \rightarrow 2$ transition of D_2 + Ne and a detailed description of the conversion of time-of-flight spectra to cross sections are given in Sec. III. The theoretical treatment of the calculation, possible approximations involved, and the sensitivity of the data to the anisotropic potential are reviewed in Sec. IV. The determination of the potential and the comparison of the measured data with the predictions of the fitted potential and other available potentials are made in Sec. V. A discussion of the final results follows in Sec. VI.

II. EXPERIMENTAL

The details of the experimental arrangement have been described elsewhere.[7,11] Briefly, the D_2 and Ne beams which cross at 90° are produced as nozzle beams from two differentially pumped chambers. The scattered D_2 particles are detected by a double differentially pumped quadrupole mass spectrometer operating at pressures lower than 10^{-10} mb. The angular dependence is measured by rotating the source assembly versus the fixed detector unit. Elastic and inelastic events are separated by time-of-flight analysis of the scattered particles using the pseudorandom chopping technique. Compared to the previously published experimental arrangement, the pumping facilities were substantially improved to produce nozzle beams at stagnation pressures up to 200 b.[21] Each of the two chambers were evacuated by an unbaffled oil diffusion pump (NRC VHS-10) backed by a roots pump and a mechanical pump with pumping speeds of 1000 m^3 h and 200 m^3 h for the primary beam chamber and 500 m^3 h and 100 m^3 h for the secondary beam chamber, respectively. This pumping system was adequate to handle a flow of 40 l/h under normal pressure conditions. The pressure in the expansion chambers never exceeded 10^{-3} mb. To compensate for the large gas flow, a gas recyling system was used for D_2. In addition the gas line could be fed to a cryostat to produce o-D_2. The details of this convertor are described in Ref. 22. The actual data of the beam arrangement and the operating conditions are given in Table I. The high pressure could only be used for the D_2 beam. For Ne the pressure range is restricted due to possible condensation. The new pumping arrangement provided a threefold improvement in the apparatus compared to the previous arrangement[11]:

(i) Due to the high intensity of these beams the accumulating time was reduced by a factor of 25.

(ii) The velocity resolution $\Delta v/v$ was improved by a factor of 2, being now mainly limited by flight path uncertainty.

(iii) The rotational temperature $T_r = 70$ K ensures that 89% of the o-D_2 molecules are in $j=0$, which is about a factor of 2 improvement.

It is interesting to note that in spite of the extreme expansion, the speed ratio for D_2 is only $S=37$, whereas we achieved in the same experimental arrangement $S = 220$ for He.[14] This is obviously due to the small influence of the rotational degrees of freedom on the translational distribution which nevertheless reaches the very low temperature $T_\parallel = 0.8$ K.

The very important populations of the rotational energy levels are obtained by an energy balance of the parent D_2 beam which gives

$$H_0 + E_{\rm rot}(T_0) = \tfrac{1}{2}mu^2 + \tfrac{5}{2}kT_\parallel + E_{\rm rot}(T_r)\,, \qquad (1)$$

where k is the Boltzmann constant, T_0 the source temperature, H_0 the enthalpy without rotational energy, $E_{\rm rot}$ the rotational energy, m the mass, u the mass flow velocity, and $T_\parallel$ the temperature after the expansion parallel to the beam direction. It is assumed that the perpendicular temperature is equal to $T_\parallel$.

The left hand side of Eq. (1) is known from the equilibrium condition before the expansion from the measured T_0. The first two terms of the right hand side can be measured by velocity analysis of the beam. Thus, $E_{\rm rot}(T_r)$ can be determined. It should be noted that H_0 cannot be approximated by $\frac{5}{2}kT_0$ since under the present experimental conditions, real gas effects cannot be neglected. Thus we use the tables of Ref. 23 for p-H_2, but only for the part of the enthalpy independent of the rotational energy. The experimental results for $E_{\rm rot}(T_r)$ are 2.45 meV for o-D_2 and 3.56 meV for n-D_2. To relate these values to level populations we assume a Boltzmann distribution and calculate the rotational energy $E_{\rm rot} = \sum_j E_j g_j \exp(-E_j/kT_r)/\sum_j g_j \exp(-E_j/kT_r)$ for a rotational temperature T_r using the known energy levels E_j.[24] The results are given in Table I. This assumption is justified by the fact that the temperatures are so low that we deal with a simple two state problem where one may describe the level population by the temperature alone. A very recent direct measurement of the level population of n-D_2 nozzle beams by Raman scattering confirms this interpretation.[25] Although a measurement at much lower pressures ($p_0 = 2.96$ b) from 80 μm nozzles gives level populations expressed by temperatures[26] ($T_{02} = 136$ K, $T_{12} = 138$ K, $T_{04} = 152$ K, and $T_{15} = 200$ K for $T_0 = 293$ K) which deviate from an equilibrium distribution characterized by a single temperature, only the higher states are really affected and relax somewhat slower. Under the experimental conditions of the present experiment ($p_0 = 195$ b, $T_r = 62$ K) it is rather improbable that the states $j=4$ or $j=5$ have any influence on the result since they are not populated at all even if they should relax appreciably slower than the other states. The main problem of the present pro-

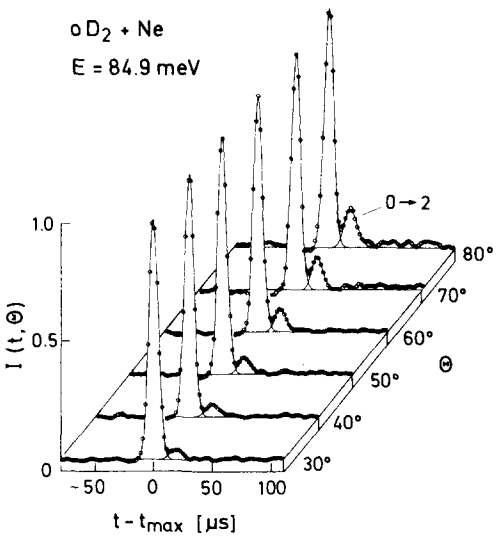

FIG. 1. Measured time-of-flight distributions for o-D_2 + Ne for different laboratory deflection angles. The peaks correspond to the elastic $0 \rightarrow 0$ and $2 \rightarrow 2$ transitions (normalized to 1) and the inelastic $0 \rightarrow 2$ transitions of D_2.

cedure is the experimental uncertainty involved since two large numbers are substracted from each other. If the two energies are measured to within 0.6% the resulting error in the level population is $p_0 = 0.89 \pm 0.04$ for o-D_2 and $0.62 \pm {}^{0.04}_{0.06}$ for n-D_2.

III. EXPERIMENTAL RESULTS AND DATA EVALUATION

A. Experimental results

The measured time-of-flight distributions of o-D_2 scattered from Ne are shown in Fig. 1 as a function of the laboratory scattering angle Θ. Each spectrum shows two peaks, at the left the elastic peak, which is normalized to one, and a well separated inelastic peak to the right corresponding to rotational excitation $j = 0$ to $j = 2$. The accumulating time for each spectrum varied from 1 h at small angles to 4 h at large angles. The result clearly shows that the transition probability increases with increasing deflection angle as is the case for HD + Ne.[11] Contrary to the HD + Ne system the transition probability is about a factor of 3 smaller than the $j = 0$ to $j = 1$ transition, in spite of the fact that the present data are obtained at $E = 84.9$ meV, which is a factor of 3 larger than the energy of the HD + Ne experiment. Similar results have been obtained for n-D_2 scattered from the same target atom Ne. According to the difference of the population in $j = 0$, the inelastic transition probabilities are smaller by a factor $\frac{2}{3}$ and, in some of the spectra, very small peaks appear corresponding to $j = 1$ to $j = 3$ transitions.[13]

B. Data analysis

Now we have to relate the measured time-of-flight distribution functions in the laboratory system to the differential cross sections for single rotational transitions in the center of mass system. Although the measured time-of-flight spectra show well-resolved peaks, one should consider the influence of the different averaging processes of the apparatus very carefully. Using the procedure described in detail in Ref. 14, the scattered beam number density (particles per cm^3 at a given laboratory angle Θ and a final velocity v_f) for a transition from i to f is given by

$$N_{if}(\Theta, v_f) = n_{1i} n_2 \langle \Delta V \Delta\Omega \rangle(\Theta) \int dv_f' D(v_f, v_f') v_f'^{-1} \times \int dg\, d\vartheta \sigma_{if}(g, \vartheta) F_{if}(g, \vartheta, v_f') \ . \quad (2)$$

ϑ is the deflection angle in the c.m. system, n_{1i} and n_2 are the averaged densities of the two beams in ΔV. g is the relative velocity. $\langle \Delta V \Delta\Omega \rangle(\Theta)$ accounts for the finite dimensions of the scattering center and the detector and v_f^{-1} for the velocity dependence of the detection. σ_{if} is the differential cross section in the c.m. system for the transition $i \rightarrow f$. $D(v_f, v_f')$ is a dimensionless transmission function of the velocity analyzer which also accounts for the finite ionization volume. The key point of the present formulation is the distribution function $F_{if}(g, \vartheta, v_f)$. This function which contains such factors as the relative velocity g, the Jacobian for the transformation from the c.m. to the lab system $J = u_f^2 / v_f^2 \cos(u_f, v_f)$, the distribution function of the c.m. variables g, ϑ, and the final velocities v_f caused by the velocity and angular spread of the two intersecting beams. It is also marked by the indices "*if*" since the distribution may be different for different transitions. Since in the present case we are only interested in the distribution of final velocities, the integration over ϑ and g is carried out and gives

$$N_{if}(\Theta, v_f) = \bar{v}_f^{-1} K p_i G_{if}(v_f) \sigma_{if}(\bar{\vartheta}, \bar{g}) \bar{J}_{if} \ , \quad (3)$$

where $K = n_1 n_2 \langle \Delta V \Delta\Omega \rangle(\Theta) \bar{g}$, $n_1 = \sum_i n_{1i}$, and $p_i = n_{1i}/n_1$. The functions G_{if} are normalized to $\int G_{if}(v_f) dv_f = 1$. In obtaining (3) it is assumed that the cross section varies only slowly in the narrow velocity range of the distribution function and is equal to the cross section at the maximum of the distribution functions for the g and ϑ values. This step is justified because in the measured monotonic angular range no additional averaging effects occur. It is not correct in the oscillatory part of the cross section where the explicit g dependence of the cross section must be used for the calculation of the distribution function G_{if}. For practical reasons only the functions $G_{\Delta E}(v_f)$ have to be calculated, since transitions which belong to the same $\Delta E = E_f - E_i$ cannot be distinguished in the experiment. The results for $G_{\Delta E}$ from a Monte Carlo simulation for the present experimental conditions are characterized as follows. The distribution function can be approximated by a Gaussian with a nearly constant full-width at half-maximum of 5% for the elastic and 4.8% for the $0-2$ transition centered very near to the nominal position $\bar{v}_f$ calculated from the known ΔE and the peak values of v_1 and v_2. The contributions to the half-width of the elastic peak are equally due to the finite width of the velocity distributions (3.4%), the finite ionization region (2.7%), and to the shutter function and channel width of the time-of-flight analyzer (1.8%).

Now the measured spectra which consist of several transitions ΔE are fitted to the calculated functions $G_{\Delta E}$

$$N(\Theta, v_f) = \bar{v}_f^{-1} \sum_{\Delta E} A_{\Delta E}(\Theta) G_{\Delta E}(\Theta, v_f) \tag{4}$$

giving rise to the amplitudes $A_{\Delta E}(\Theta)$. To allow for small errors between measured and simulated velocity distributions $G_{\Delta E}$ we fixed only the ratios of the calculated half-widths and regarding the restrictions of kinematics also small changes in the peak positions were admitted. The background consists of a large constant contribution and a small velocity dependent part which is due to effusive particles from the scattering chamber. This part is carefully measured and subtracted from the measured spectra. Inspection of Eq. (3) shows that the $A_{\Delta E}$ are given by

$$A_{\Delta E}(\Theta) = K \sum_{if} p_i \bar{J}_{if} \sigma_{if}(\vartheta, \bar{g}) \ , \tag{5}$$

where the summation is to be carried out only over transitions which belong to the same ΔE. To eliminate long time fluctuation of the beams the $A_{\Delta E}$ are normalized to the total differential signals at the same angle Θ,

$$\begin{aligned} N_{\text{tot}}(\Theta) &= \int N(\Theta, v_F) dv_F \\ &= \sum_{\Delta E} A_{\Delta E} \langle v_f^{-1} \rangle_{\Delta E} \ , \end{aligned} \tag{6}$$

measured independently in a lock-in experiment.

In the present study, three ΔE transitions have been observed which belong to the elastic case ($\Delta E = 0$), the $0 \rightarrow 2$ transition ($\Delta E = 22.2$ meV), and the $1 \rightarrow 3$ transition ($\Delta E = 36.9$ meV). Since the states $j = 0$, 1, and 2 are populated initially we have, according to Eq. (5)

$$\begin{aligned} A_{el}/\bar{J}_{el} &= K[p_0 \sigma_{00}(\vartheta) + p_1 \sigma_{11}(\vartheta) + p_2 \sigma_{22}(\vartheta)] \ , \\ A_{02}/\bar{J}_{02} &= K p_0 \sigma_{02}(\vartheta) \ , \\ A_{12}/\bar{J}_{13} &= K p_1 \sigma_{13}(\vartheta) \ . \end{aligned} \tag{7}$$

The proportionality factor K is the same in all cases.

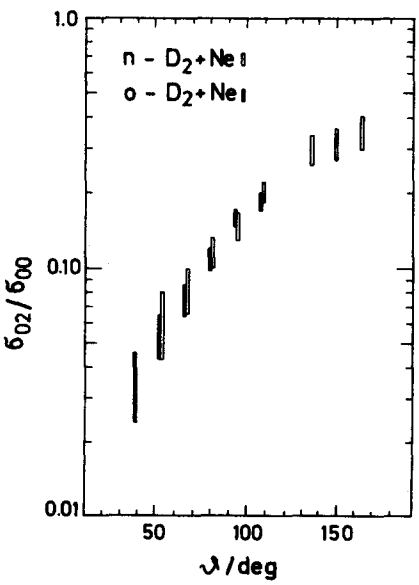

FIG. 2. Measured cross section ratios for n-D_2 + Ne and o-D_2 + Ne as a function of the average center-of-mass deflection angle.

TABLE II. Measured differential cross sections in arbitrary units. Here, ϑ_{if} are c.m. scattering angles for the transition $i \rightarrow f$.

θ (deg)	ϑ_{00}	ϑ_{02}	ϑ_{13}	σ_{00}	σ_{02}	σ_{13}
30	38.4	36.4	34.1	1473 ± 20	54.5 ± 18	···
40	52.1	50.6	49.1	1043 ± 15	60.5 ± 11	16 ± 18
50	66.0	65.1	64.3	814 ± 10	64.5 ± 8.5	22 ± 13
60	80.0	79.8	79.7	660 ± 8	74.0 ± 7.0	20 ± 11
70	94.0	94.5	95.1	555 ± 7	86.0 ± 6.5	27 ± 11
80	108.0	109.1	110.4	487 ± 7	94.5 ± 6.0	28 ± 9
100	135.4	137.8	140.4	391 ± 10	116 ± 14	41 ± 16
110	148.5	151.5	154.7	366 ± 10	116 ± 14	38 ± 17
120	161.2	164.7	168.4	350 ± 10	124 ± 16	73 ± 25

Since the level populations are known the inelastic cross sections are easily obtained. The individual elastic cross section σ_{00}, however, can only be derived from (7) with help of the knowledge of σ_{11} and σ_{22}. Generally they will not deviate very much from each other. Since the inelastic cross sections are known from experiment it is a reasonable assumption to use the identity

$$\sigma_{00}(\vartheta) + \sigma_{02}(\vartheta) = \sigma_{11}(\vartheta) + \sigma_{13}(\vartheta) = \sigma_{22}(\vartheta) + \sigma_{24}(\vartheta) \tag{8}$$

which accounts for the conservation of channel cross sections. Under the assumption that the transformations from the c.m. system to the lab system for the inelastic transitions will give nearly the same deflection angle as for the elastic part, we have using (7) and (8)

$$K\sigma_{00}(\vartheta) = \frac{A_{el}}{\bar{J}_{el}}(\Theta) - \frac{(p_1 + p_2)}{p_0} \frac{A_{02}}{\bar{J}_{02}}(\Theta) + \frac{A_{13}}{\bar{J}_{13}}(\Theta) \ . \tag{9}$$

Since we could not detect any $2 \rightarrow 4$ transitions A_{24} has been set equal to zero. It is obvious from Eqs. (7) and (9) that cross section ratios do not depend on the constant K. With the known p_i from Table I and the experimental $A_{\Delta E}$ we are able to determine σ_{02}/σ_{00} for both series of measurements for o-D_2 and n-D_2. The results are shown in Fig. 2. For convenience, the data are interpolated and plotted for the average value of ϑ_{00} and ϑ_{02}. The cross section ratios agree well within their experimental errors which gives us confidence in the data evaluation procedure. The errors are partly due to the statistical noise of the measured spectra and to a systematic error from the tail of the elastic distribution which influences very small inelastic contributions. As a final result we use the average value of the two ratios. Individual cross sections have been obtained from Eqs. (7) and (9). The final results are given in Table II.

IV. CALCULATIONS

To compare the experimental results with theoretical predictions we solve the coupled Schrödinger equations for an anisotropic interaction potential. For the energy range and the rotational transitions under study it is sufficient to include only one anisotropic term in the usual expansion of the potential surface in Legendre polynomials:

$$V(R, \gamma) = V_0(R) + V_2(R) P_2(\cos\gamma) \ . \tag{10}$$

R is the distance between the atom and the center of mass of the diatomic molecule and γ is the angle between the molecular axis and R. As for the potential model

the realistic Hartree–Fock dispersion form was chosen[27,16] which gives for $i=0,2$

$$V_i = A_i \exp(-b_i R) - (C_{6i}R^{-6} + C_{8i}R^{-8} + C_{10i}R^{-10})F(R) , \tag{11}$$

$$F(R) = \exp[-(2.29R_d/R - 1)^2], \quad R < 2.29R_d$$
$$= 1, \quad R \geq 2.29R_d .$$

The dispersion coefficients are known from Ref. 16:

$$C_{60} = 5.06 \text{ eV Å}^6 , \quad C_{62} = 0.4756 \text{ eV Å}^6 ,$$
$$C_{80} = 21.54 \text{ eV Å}^8 , \quad C_{82} = 6.0312 \text{ eV Å}^8 , \tag{12}$$
$$C_{100} = 113.72 \text{ eV Å}^{10} , \quad C_{102} = 31.842 \text{ eV Å}^{10} .$$

R_d is estimated by $R_d = (C_{80}/C_{60})^{1/2} = 2.063$ Å. The parameters A_i and b_i are usually treated as free parameters and are determined from the experiment.

First we have tested the coupled states (CS) approximation[28] versus the exact close coupling (CC) formalism. Figure 3 shows the result of a calculation for the $j=0$ to $j=2$ transition of D_2 scattered from Ne at $E = 84.9$ meV. A basis of $j=0, 2, 4$ proved to give fully converged results. As potential model we used V_0 of Ref. 29 and V_2 of the form of Eq. (11) with the parameters given in Eq. (12) and $A_2 = 230.47$ eV, $b_2 = 3.832$ Å^{-1}. Contrary to the results of HD + Ne,[11] the two follow each other very closely. The deviations are less than 0.2% for angles larger than 60° and less than 1% for angles $30° < \vartheta < 60°$. Only for very small angles do significant deviations occur. This behavior is expected since the anisotropy of the system mainly occurs in the repulsive part of the potential. Since we are only interested in results outside the oscillatory regime of the cross section, the CS approximation is used for all subsequent calculations shown in this paper.

The influence of the potential form of Eq. (10) has been tested by adding a V_4 term to the potential. The cross section σ_{02} becomes smaller with increasing strength of the V_4 term. Probably the σ_{04} cross section

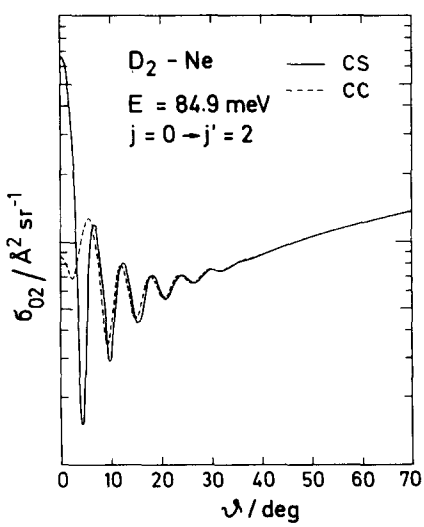

FIG. 3. Calculated differential cross sections for the inelastic $0 \rightarrow 2$ transition in the coupled-states (CS) approximation and the exact close-coupling (CC) formalism.

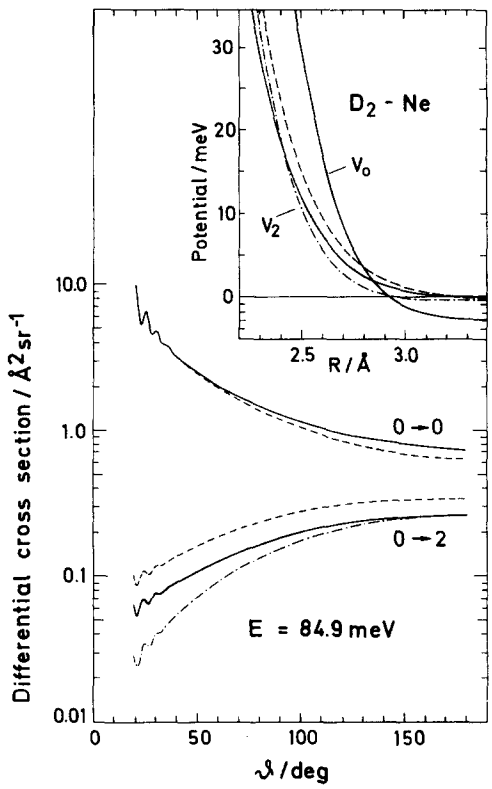

FIG. 4. Calculated differential cross sections (CS approximation) for the $0 \rightarrow 0$ and $0 \rightarrow 2$ transitions of D_2 + Ne for the three different anisotropic potentials V_2 and fixed V_0 as shown in the upper part of the figure. Note the complete mapping of $V_2(R)$ and $\sigma_{02}(\vartheta)$.

is increased at the expense of the σ_{02} cross section. However, for a realistic contribution $V_4 = 0.1\,V_2$,[30] the inelastic cross sections decrease by only 2%, justifying neglect of this contribution.

To study the influence of the nonspherical potential part $V_2(R)$ on the $j=0 \rightarrow j=2$ transitions we have performed calculations for a fixed isotropic part ($A_0 = 890$ eV, $b_0 = 3.9$ Å^{-1}) and three anisotropic parts $V_2(R)$ differing in the amplitude ($A_2 = 360$ eV, $b_2 = 4.0$ Å^{-1}, $A_2 = 396$ eV, $b_2 = 4.0$ Å^{-1}) and in the slope ($A_2 = 2410$ eV, $b_2 = 4.8$ Å^{-1}) of the repulsive part but using the same attractive part of the potential [Eq. (12)]. The result as displayed in Fig. 4 shows a nearly complete mapping of the structure of the V_2 potential on the σ_{02} cross section. Thus the large angle part of the cross section for the $j=0$ to $j=2$ transition is an extremely sensitive probe for the repulsive part of the pure anisotropic interaction. This behavior may be traced back directly to the behavior of the corresponding S-matrix elements which are plotted as a function of the angular momentum L in Fig. 5. The square of the modulus which is proportional to the transition probability is not larger than 0.35 and is a smooth nonoscillatory function of L showing just the behavior of the cross section. The related angles are given by the derivative of the phase of the S-matrix element with respect to the angular momentum, the quantum analog to the classical deflection function. For convenience, the angles of the elastic and the inelastic channels are given. The connection between the S-matrix

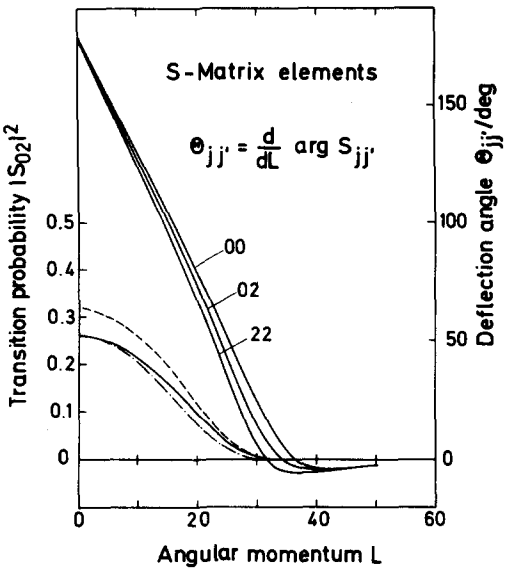

FIG. 5. Quantum deflection function (right hand scale) and transition probability (left hand scale) as a function of the angular momentum parameter L based on the calculation shown in Fig. 4. The different curves (solid, dashed, dashed-dotted lines) correspond to the different potentials shown in Fig. 4.

elements and the potential can be rationalized by distorted wave integrals as described in detail in Ref 31. This approximation is indeed valid for the small transition probabilities of the studied transition. Indirectly we conclude from Figs. 4 and 5 that the anisotropic potential is probed from the potential minimum (the zero point of the deflection function) around 3.2 Å to the region around 2.3 Å, which is just very near to the classical turning point R_t of the isotropic potential. This fact can also be explained by the distorted wave integrals

$$S_{02} \sim \sin\left(\int_0^\infty \psi_{i2}^{(0)} V_2 \psi_{i0}^{(0)} dR\right) \tag{13}$$

since the wave function ψ_{ii} drops exponentially near the turning point of V_0. Equation (13) gives directly the proportionality of S_{02} to V_2. The dependence of the inelastic transition on V_0 depends only on the position of R_t. If V_0 increases, R_t increases leading to a smaller value of V_2. Thus for an exponential potential, the transition depends on the ratio of V_2 to V_0.

V. COMPARISON OF EXPERIMENT AND THEORY

The following data sets are used to determine the complete potential surface for D_2Ne according to Eq. (10):

(i) The total differential cross sections $[\sigma(0 \to 0) + \sigma(0 \to 2)]$ for $D_2 + Ne$ (Ref. 14 and this work);

(ii) the rotationally inelastic differential cross sections $\sigma(0 \to 1)$ for $HD + Ne$ (Ref. 11); and

(iii) the rotationally inelastic differential cross sections $\sigma(0 \to 2)$ for $D_2 + Ne$ presented in this work.

The potential model used is that of Eq. (11) where we take the dispersion coefficients of Eq. (12) for granted. Thus we are left with the determination of four free parameters A_0, b_0, A_2, b_2 which describe the minimum and repulsive part of the isotropic part V_0 and the anisotropic part V_2, respectively. In practice we proceed as follows. In a *first step* the total differential cross section σ_{tot} for $D_2 + Ne$ is evaluated like an elastic atom–atom cross section (one channel calculation). Such a treatment is especially valid in the small angle oscillatory regime since the inelastic contribution is negligible there. This procedure gives a first approach to $V_0^{(1)}$. Then, in a *second step* $V_0^{(1)}$ and the state-to-state cross sections $\sigma(0 \to 0)$ and $\sigma(0 \to 2)$ for $D_2 + Ne$ are used to determine $V_2^{(1)}$ via a coupled channel calculation. In a *third step* $V_2^{(1)}$ is used to derive a very reliable $V_0^{(2)}$ based on coupled channel equations for the total differential cross section of $D_2 + Ne$ and the $\sigma(0 \to 1)$ differential cross section of $HD + Ne$. The information content of these input data is to certain extent complementary. Whereas the oscillatory part of the sum cross section $\sigma_{tot} = \sigma(0 \to 0) + \sigma(0 \to 2)$ for $D_2 + Ne$ is especially sensitive to the position and the form of V_0 near the zero point, the $\sigma(0 \to 1)$ for $HD + Ne$ probes with high accuracy the slope of V_0 in the repulsive region.[11] The use of the total cross section instead of the pure elastic channel $\sigma(0 \to 0)$ in such a procedure is to be preferred, since the latter (due to the coupled channels) is stronger influenced by V_2 than σ_{tot}.[31] In a *last step* this very reliable $V_0^{(2)}$ is now used for the final determination of $V_2^{(2)}$ based on the $\sigma(0 \to 2)$ cross sections of $D_2 + Ne$. As shown in Sec. IV, this gives a complete mapping of the cross section to the potential. The last two steps are repeated so as to obtain a best fit to the data. As a criterion of the quality of the fit the root mean squared deviation (RMS) has been employed,

$$\mathrm{RMS} = \left[\frac{1}{N-1}\sum_{i=1}^{N}\left(\frac{\sigma_{calc} - \alpha\sigma_{expt}}{\alpha\Delta\sigma_{expt}}\right)^2\right]^{1/2}, \tag{14}$$

where N is the number of data points. For the total cross section and the elastic transitions, the constant α serves to adjust the absolute value of the calculations and the relative value of the experiments. For the inelastic transitions ($0 \to 1$ of $HD + Ne$ and $0 \to 2$ of $D_2 + Ne$) the α of the corresponding elastic transition is used so that two absolute quantities are compared. For D_2Ne $\alpha = 0.002\,25$ is obtained which transforms the data of Table II into absolute quantities. The final result for the complete potential is given in Table III and Fig. 6. The errors of R_{00}, b_0, A_2, and b_2 are derived from the original fitting procedure whereas those of A_0 and R_{02} are estimated from these results. The corresponding RMS values are listed in Table IV. For the total differential cross section of $D_2 + Ne$ we have provided two entries, one for the entire and one for the large angle range which is only sensitive to b_0. The comparison of the calcula-

TABLE III. Potential parameters.

	ϵ_i (meV)[a]	R_{mi} (Å)[b]	R_{oi} (Å)[c]	A_i (meV)	b_i (Å^{-1})
V_0	2.85	3.30	2.92 ± 0.02	890 ± 37	3.9 ± 0.1
V_2	0.27	3.56	3.19 ± 0.07	360 ± 18	4.0 ± 0.3

[a]Well depth. [b]Minimum position. [c]Zero point.

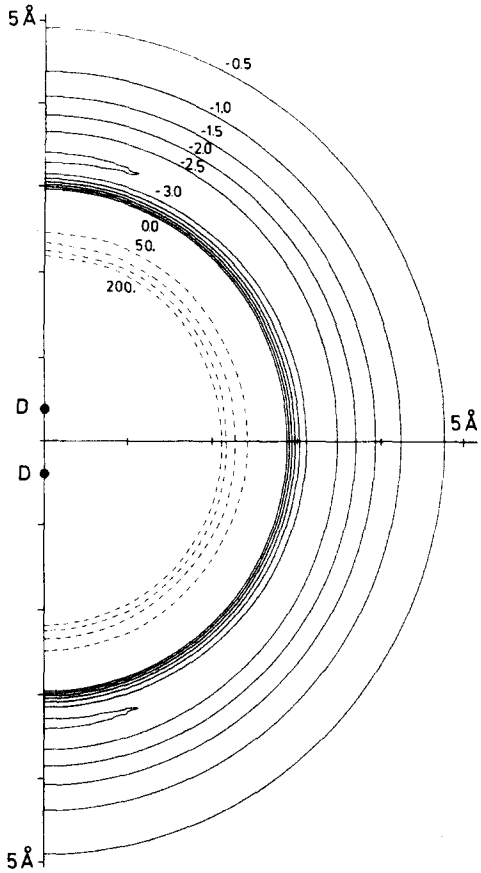

FIG. 6. Polardiagram of the potential surface for D_2 + Ne obtained from experiment. The solid lines mark the attractive part, the dashed lines the repulsion. The numbers give the energies in meV.

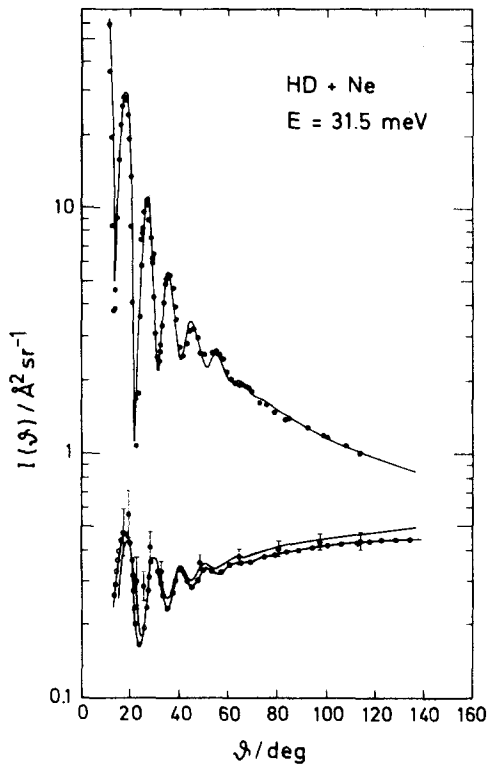

FIG. 7. Measured differential cross sections for the $0 \rightarrow 0$ and $0 \rightarrow 1$ transitions of HD+ Ne (Ref. 11) and calculations in the CS approximation based on the best fit potential of this work (solid line) and the potential obtained by an inversion procedure of the $0 \rightarrow 2$ transitions of D_2 (Ref. 20) with V_0 from Ref. 14 (circles on a solid line). For the elastic cross sections the last result is not shown, since it coincides with the solid line.

tions based on this potential with the experimental results for the $0 \rightarrow 0$ and $0 \rightarrow 1$ transitions of HD + Ne and the $0 \rightarrow 0$ and $0 \rightarrow 2$ transitions of D_2 + Ne is shown in Figs. 7 and 8, respectively. The calculated results are given by the solid lines. The fit is in nearly perfect agreement with the data. Only the two low angle points of the weak $0 \rightarrow 2$ transition for D_2 + Ne are slightly outside the error bars. We have also calculated the velocity dependence of the integral cross section for selective orientations $A = (Q_{mj=1} - Q_{mj=0})/Q_{mj=1}$ as measured by Zandee and Reuss.[15] In contrast to our data, these data are mainly sensitive to the attractive part of the potential. The result of the calculation based on our potential is shown in Fig. 9 by the solid line.

The fit is not perfect; however, it is better than for any other potential available in the literature as can be seen from the RMS values of Table IV. Thus we conclude that the potential surface determined in this work describes all available molecular beam data. It should

TABLE IV. Root mean squared deviations.

Property	System data	Present	TT[a]	DG[b]	LC[c,h]	RFBK[d]
Differ. total	D_2Ne Buck *et al.*[e]	2.26	4.32	8.53	12.65	13.78
large angles	D_2Ne Buck *et al.*[e]	1.25	2.37	1.44	8.43	3.06
Differ. $0 \rightarrow 1$	HDNe Buck *et al.*[f]	0.87	2.14	1.38	3.15	1.67
Differ. $0 \rightarrow 2$	D_2Ne this work	0.61	1.49	0.56	6.12	1.04
Int. $(Q_0 - Q_1)/Q_0$	H_2Ne Zandee *et al.*[g]	2.62	3.46	5.70	3.69	8.32

[a]Reference 16.
[b]Reference 17.
[c]Reference 18 (potential BC_3).
[d]Reference 19.
[e]Reference 14.
[f]Reference 11.
[g]Reference 15.
[h]For potential BC_0 of Ref. 33 we have RMS values as follows: 12.28, 5.8, 2.49, 4.16, 3.69.

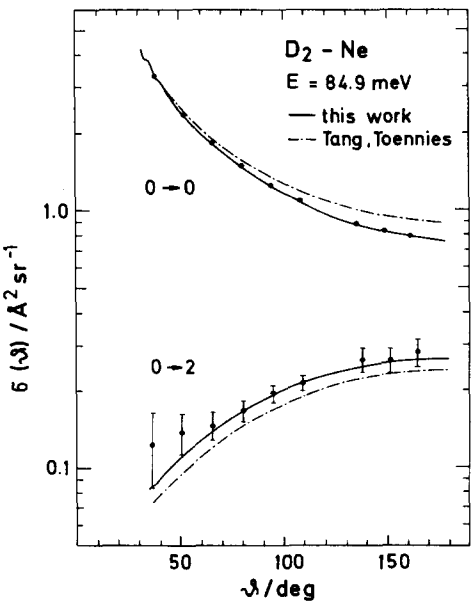

FIG. 8. Measured differential cross sections for the $0 \rightarrow 0$ and $0 \rightarrow 2$ transitions of $D_2 + Ne$ and calculations based on the best fit potential of this work (solid line) and the potential of Ref. 16 (dashed dotted line).

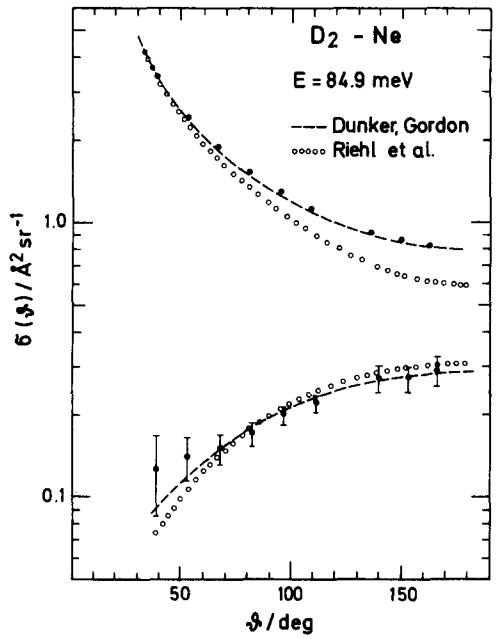

FIG. 10. Measured differential cross sections for the $0 \rightarrow 0$ and $0 \rightarrow 2$ transitions of $D_2 + Ne$ and calculations based in the potentials of Ref. 17 (dashed line) and Ref. 19 (open circles). V_2 is plotted in Fig. 11.

be reliable in the range from 2.4 to 5.0 Å which includes the attractive part and the repulsive part near the minimum. The general form of this potential is shown in Figs. 6 and 11. As expected, the anisotropy is rather small, leading to a slightly more repulsive linear configuration compared to the perpendicular configuration. As for the attractive part, the well in the parallel configuration is slightly deeper (0.3 meV) than in the perpendicular configuration, in agreement with the results of the spectroscopy of the van der Waals complex where a loosely bounded nearly free rotating complex was found.

Expressed in terms of the usual expansion in Legendre polynomials [Eq. (10)], the V_2 term exhibits nearly no minimum (it is always smaller than $0.1\,V_0$), crosses the V_0 term at 2.85 Å, and reaches $0.37\,V_0$ at 2.4 Å. Because of this behavior the main coupling occurs in the repulsive part of the potential which leads to the largest transition probabilities in the backward direction.

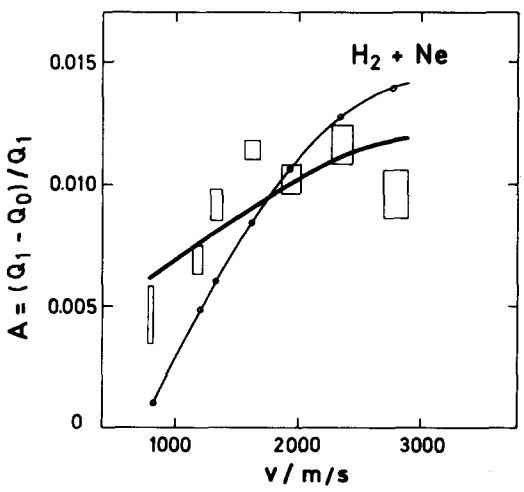

FIG. 9. Measured anisotropy of the velocity dependence of oriented H_2 molecules scattered from Ne (Ref. 15) and calculations in the DW approximation based on the best fit potential of this work (solid line) and the result of the inversion (Ref. 20) (circles on the solid line).

VI. DISCUSSION

Since the present investigation is the first attempt to analyze state-to-state rotationally elastic and inelastic differential cross sections in terms of a complete—isotropic and anisotropic—potential we can only compare these predictions with the results obtained from other sources. There are the detailed analysis of the infrared spectra of the van der Waals complexes,[17,18] a study of NMR relaxation in gases,[19] and a semiempirical potential model where long range dispersion coefficients and Hartree–Fock–repulsion terms are added.[16]

Since the data of Zandee and Reuss[15] have been used in our analysis as contraints for the attractive part of the potential, an additional comparison with their potentials based on the simple Lennard-Jones 12–6 form is not necessary. The result of the comparison of the experimental beam data to calculations based on these potentials are expressed by the root mean squared deviations of Eq. (14) and listed in Table IV. At a first glance none of these potentials gives as good values as the potential obtained in the present work. To illustrate the deviations from the $0 \rightarrow 0$ and $0 \rightarrow 2$ transitions of $D_2 + Ne$ the results are plotted in Figs. 8 and 10. As for similar plots of the total differential cross section for $D_2 + Ne$ we refer to Ref. 14, for the $HD + Ne$ system to Ref. 11 and for the integral cross sections of oriented molecules to Refs. 15 and 16. The anisotropic parts of the

potentials used in these calculations are displayed in Fig. 11 and the ratios V_2/V_0 in Fig. 12. The isotropic potentials V_0 appear in Refs. 14 and 16.

The semiempirical model of Tang and Toennies[16] gives the second best overall fit to the data. The differential cross sections for the $0 \rightarrow 0$ and $0 \rightarrow 2$ transitions of D_2 + Ne and the $0 \rightarrow 1$ transition of HD + Ne are only slightly outside the error bars reflecting the steeper rise of V_0 and V_2 (see Fig. 11) whereas the attractive part is almost identical to our best fit potential. Note that the smaller ratio V_2/V_0 compared to the best fit potential (see Fig. 12) is responsible for the lower $0 \rightarrow 2$ differential cross section. The relatively good predictions of the model mainly underlines that the H_2–Ne potential is well reproduced by the Hartree–Fock–dispersion form. Our potential model is of the same type. We cannot expect perfect agreement since the input data, the asymptotic coefficients, are only known to within a certain range of errors. In fact, if we take into account these errors, the deviations of the resulting potentials are larger than the errors imposed by the experimental results of the present paper.

The potentials derived from spectroscopic data by Dunker and Gordon (DG) and Le Roy and Carley (LC) behave quite differently, although they have been obtained from the same data.[32] The LC potential does not reproduce the beam data of Table IV very well, whereas the DG potential fits the $0 \rightarrow 2$ transitions of D_2 + Ne (Fig. 10) surprisingly well and the $0 \rightarrow 1$ transition of HD + Ne[11] reasonably well. First of all we should point out that all

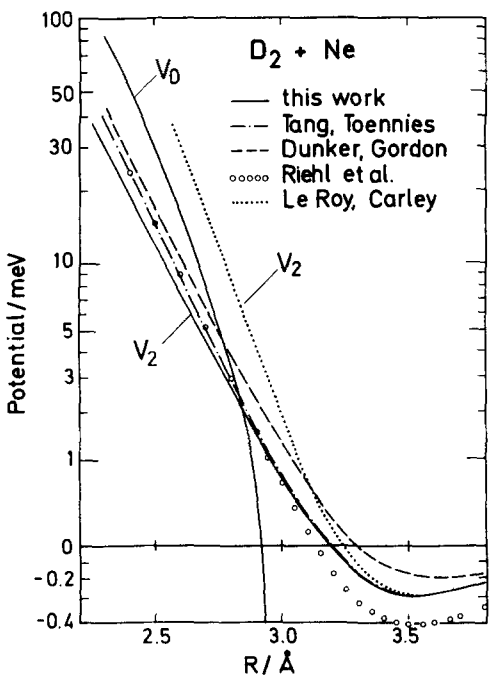

FIG. 11. Anisotropic potentials $V_2(R)$ for $D_2(H_2)$ + Ne: ——, solid line, this work; -·-, dash dotted, Ref. 16; ----, dashed, Ref. 17; ooo, open circles, Ref. 19; ····, dotted, Ref. 18. For comparison also the best isotropic potential $V_0(R)$ (Ref. 14) is given. Note the logarithmic scale which is in fact $10 \log(V_2 + 0.8)$.

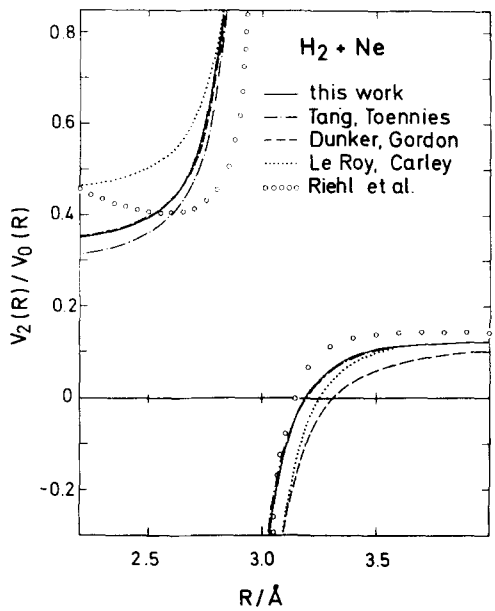

FIG. 12. Ratio of $V_2(R)/V_0(R)$ for $D_2(H_2)$ + Ne. The notation is that of Fig. 11.

the spectroscopic data are only sensitive to the attractive part of the potential which is not probed in the differential cross sections presented in this paper. In addition, for H_2, D_2–Ne nearly no information about the potential anisotropy could be extracted from the existing spectra.[17,18] Thus all the numbers of Table IV rely on extrapolations which are much better for the DG potential than for the LC potential. In fact, if we use instead of the recommended BC_3 potential of LeRoy and Carley[18] the BC_0 potential of Carley,[33] which gives a similar good fit to the spectroscopic data, the RMS values of Table III improve slightly since this potential is much weaker in the repulsive region. Also the good agreement of the $0 \rightarrow 2$ transitions of D_2 + Ne, which is due to the correct V_2/V_0 ratio (see Fig. 12), must be regarded as fortuitous since V_0 is not able to reproduce the total differential cross section because of too large R_0 and ϵ values.

It is interesting to note that the potential of Riehl *et al.*[19] derived from bulk properties gives a reasonable fit to the inelastic $0 \rightarrow 2$ transition (see Figs. 10 and 12). The zero point of V_2 to which the data are very sensitive is near to the one determined in this work (see Fig. 11). A last comparison is possible for the results of a very recent inversion procedure[20] where the same data presented here have been used to determine the anisotropic V_2 potential directly from the measured data without assuming a special potential form. The comparison of the two potentials is displayed in the upper part of Fig. 13. The circles are based on measured points, whereas the quadrangles are extrapolated. The points are in excellent agreement up to 2.6 Å. This result indicates that within the probed R range (i) the potential form used in the fitting procedure is correct, and (ii) the approximations involved in the inversion procedure are justified. It should be noted that the inversion procedure

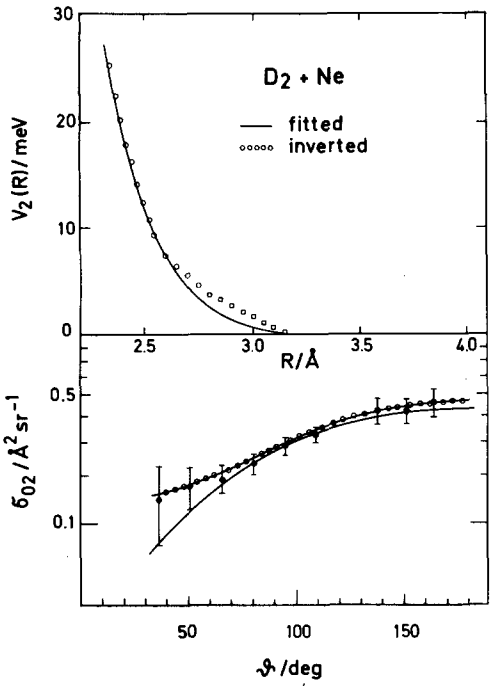

FIG. 13. Upper part: $V_2(R)$ obtained by a best fit procedure in this work (solid line) and by an inversion procedure of Ref. 20 (open circles). The open quadrangles are extrapolated points. Lower part: Measured $0 \rightarrow 2$ transitions of $D_2 + Ne$ of this work and CS calculations based on the two potentials shown in the upper part: ——, solid fit potential; ooo, circles on a solid line; potential obtained by inversion.

gives without additional effort not only the range of the potentials but also the errors based on the experimental uncertainties: 10% at 2.7 Å, 4% at 2.5 Å, and 7% at 2.4 Å, in good agreement with the results of Table III. For the last three points (the circles in Fig. 13) of the potential obtained by inversion deviations occur. Now it is interesting to see if these deviations are due to the procedure or due to the data at low angles. Thus we have recalculated the cross sections assuming this potential. The result is shown in the lower part of Fig. 13. Indeed, the curve based on the inversion of the measured data follows much closer the low angle data points than the curve based on the fitting procedure. Thus we conclude that the inversion procedure is a self-consistent scheme whereas the potential model used in the fitting procedure does not seem to be flexible enough to reproduce this data. In order to test this new potential we have also calculated the $0 \rightarrow 1$ transition of HD + Ne and the difference of the integral cross sections for two different orientations. The results are displayed in Figs. 7 and 9. Whereas the $0 \rightarrow 1$ transition is reproduced within the error bars, the integral cross sections are not as well predicted as by the best fit potential. Thus there is a slight inconsistency of the high velocity data points of Zandee and Reuss and our low angle data points of the $0 \rightarrow 2$ transitions of $D_2 + Ne$ which are both very difficult to measure. With regard to these experimental difficulties and the fact that most of the points agree with each other we conclude that the potential determined in this work for the isotropic and the anisotropic interaction of D_2 (H_2) + Ne is the best one available at the present time from molecular beam data.

ACKNOWLEDGMENTS

We thank G. Drolshagen for providing a copy of his program for the calculation of integral cross sections for different orientation. All calculations have been performed at the GWD, Göttingen. The continuous support of this work by Professor H. Pauly is gratefully acknowledged. U.B. and J.S. acknowledge a grant from the Niedersächsischer Minister für Wissenschaft und Kunst.

[1]For a review on the experiments performed until 1977, see M. Faubel and J. P. Toennies, Adv. At. Mol. Phys. 13, 229 (1977).
[2]H. Thuis, S. Stolte, and J. Reuss, Comments At. Mol. Phys. 8, 123 (1979).
[3]P. J. Dagdigian, B. E. Wilcomb, and M. A. Alexander, J. Chem. Phys. 71, 1670 (1979).
[4]K. Bergmann, R. Engelhardt, U. Hefter, and J. Witt, J. Chem. Phys. 71, 2726 (1979).
[5]W. Schepper, U. Ross, and D. Beck, Z. Phys. A 290, 131 (1979); D. Beck, U. Ross, and W. Schepper, Phys. Rev. A 19, 2173 (1979).
[6]W. Eastes, U. Ross, and J. P. Toennies, Chem. Phys. 39, 407 (1979).
[7]U. Buck, F. Huisken, J. Schleusener, and H. Pauly, Phys. Rev. Lett. 38, 680 (1977).
[8]W. R. Gentry and C. F. Giese, J. Chem. Phys. 67, 5389 (1977).
[9]W. R. Gentry and C. F. Giese, Phys. Rev. Lett. 39, 1259 (1977).
[10]U. Buck, F. Huisken, and J. Schleusener, J. Chem. Phys. 68, 5654 (1978).
[11]U. Buck, F. Huisken, J. Schleusener, and J. Schäfer, J. Chem. Phys. 72, 1512 (1980).
[12]W. R. Gentry, in *Electronic and Atomic Collisions*, edited by N. Oda and K. Takayanagi (North–Holland, Amsterdam, 1980), p. 807.
[13]J. Andres, U. Buck, F. Huisken, J. Schleusener, and F. Torello, in *Electronic and Atomic Collisions*, edited by N. Oda and K. Takayanagi (North–Holland, Amsterdam, 1980), p. 531.
K. Takayanagi, Kyoto, 1980), p. 531.
[14]U. Buck, F. Huisken, and J. Schleusener, J. Chem. Phys. (to be published).
[15]L. Zandee and J. Reuss, Chem. Phys. 26, 345 (1977); *ibid.* 26, 327 (1977).
[16]K. T. Tang and J. P. Toennies, J. Chem. Phys. 68, 5501 (1978).
[17]A. L. Dunker and R. G. Gordon, J. Chem. Phys. 68, 700 (1978).
[18]R. J. LeRoy and J. S. Carley, Adv. Chem. Phys. (to be published); University of Waterloo, Chemical Physics Research Report CP-126, 1979.
[19]J. W. Riehl, C. J. Fisher, J. D. Baloga, and J. L. Kinsey, J. Chem. Phys. 58, 4571 (1973).
[20]R. B. Gerber, V. Buch, U. Buck, G. Maneke, and J. Schleusener, Phys. Rev. Lett. 44, 1397 (1980).
[21]G. Brusdeylins, H.-D. Meyer, J. P. Toennies, and K. Winkelmann, in *Rarefied Gas Dynamics*, edited by J. Leith Potter (1977), Vol. 51, p. 1047.
[22]M. Faubel and J. P. Toennies, J. Chem. Phys. 71, 3770 (1979).
[23]R. D. McCarty and L. A. Weber, Natl. Bur. Stand. (U.S.) Tech. Note 617 (1972).

[24]H. W. Wooley, R. B. Scott, and F. G. Brickwedde, J. Res. National Bur. Stand. 41, 379 (1948).
[25]M. Godfried and I. I. Silvera (private communication, 1980).
[26]The ratio of the level population of a two level system p_i/p_j is characterized by a temperature $T_{ij} = \Delta E/\ln(p_i g_j/p_j g_i)$.
[27]R. Ahlrichs, R. Penco, and G. Scoles, Chem. Phys. 19, 119 (1977).
[28]D. J. Kouri, in *Atom–Molecule Collisions*, edited by R. B. Bernstein (Plenum, New York, 1979), Chap. 9.
[29]J. Schleusener, Ph. D. thesis, University of Göttingen, 1978; see also Ref. 11.
[30]A. F. Wagner, A. C. Wahl, A. M. Karo, and R. Krejci, J. Chem. Phys. 69, 3756 (1978).
[31]R. B. Gerber, V. Buch, and U. Buck, J. Chem. Phys. 72, 3596 (1980).
[32]A. R. W. McKellar and H. L. Welsh, J. Chem. Phys. 55, 595 (1971); Can. J. Phys. 50, 1458 (1972).
[33]J. S. Carley, Ph. D. thesis, University of Waterloo, Canada, 1979.